Investigating the role of Tunable Nitrogen Vacancies in Graphitic Carbon Nitride Nanosheets for Efficient Visible-Light-Driven H_2 evolution and CO_2 reduction

Wenguang Tu,[†] You Xu,[†] Jiajia Wang,[‡] Bowei Zhang,[§] Tianhua Zhou,[†] Shengming Yin,[†] Shuyang Wu,[†] Chunmei Li,[†] Yizhong Huang,[§] Yong Zhou,[⊥] Zhigang Zou,[⊥] John Robertson,[∥] Markus Kraft,[▽, ○] and Rong Xu[, †, ▽]*

[†]School of Chemical & Biomedical Engineering, Nanyang Technological University, 62 Nanyang Drive, 637459, Singapore

[‡]College of Mechanics and Materials, Hohai University, Nanjing 210098, P. R.China

[§]School of Materials Science and Engineering, Nanyang Technological University, 50 Nanyang Avenue, 639798, Singapore

[⊥]Laboratory of Modern Acoustics, MOE, Institute of Acoustics, School of Physics, Nanjing University, 22 Hankou Road, Nanjing, Jiangsu 210093, P. R. China

[∥]Department of Engineering, University of Cambridge, Cambridge CB3 0FA, U.K.

[▽]C4T CREATE, National Research Foundation, CREATE Tower 1 Create Way, 138602, Singapore

[○]Department of Chemical Engineering and Biotechnology, University of Cambridge

Cambridge CB2 3RA, UK

KEYWORDS: Keywords: photocatalysis, g-C_3N_4, nitrogen vacancy, midgap states

ABSTRACT: Vacancy engineering, i.e. self-doping of vacancy in semiconductors, has become a commonly used strategy to tune the photocatalytic performances. However, there still lacks fundamental understanding of the role of the vacancies in semiconductor materials. Herein, the g-C_3N_4 nanosheets with tunable nitrogen vacancies are prepared as the photocatalysts for H_2 evolution and CO_2 reduction to CO. Based on both experimental investigation and DFT calculations, nitrogen vacancies in g-C_3N_4 induce the formation of midgap states under the conduction band edge. The position of midgap states becomes deeper with the increasing of nitrogen vacancies. The g-C_3N_4 nanosheets with the optimized density of nitrogen vacancies display about 18 times and 4 times of enhancement for H_2 evolution and of CO_2 reduction to CO, respectively, compared to the bulk g-C_3N_4. This is attributed to the synergistic effects of several factors including: 1) nitrogen vacancies cause the excitation of electrons to midgap states below the conduction band edge which results in extension of the visible light absorption to photons of longer wavelengths (up to 598 nm); 2) the suitable midgap states could trap photogenerated electrons to minimize the recombination loss of photogenerated electron-hole pairs; and 3) nitrogen vacancies lead to uniformly anchored small Pt nanoparticles (1-2 nm) on g-C_3N_4, and facilitate the electron transfer to Pt. However, the over-introduction of nitrogen vacancies generates deeper midgap states as the recombination centers which results in deterioration of photocatalytic activities. Our work is expected to provide new insights for fabrication of nanomaterials with suitable vacancies for solar fuel generation.

1. INTRODUCTION

Converting solar energy to chemical energy in the form of H_2 and hydrocarbon fuels by semiconductor photocatalysts is considered as one of promising techniques to mitigate the energy crisis and global warming.[1-6] Although numerous semiconductor photocatalysts have been explored such as TiO_2,[7-9] CdS,[10-12] Zn_2GeO_4[13, 14], g-C_3N_4,[15, 16] the lack of visible-light harvesting materials and the fast recombination of photogenerated electron-hole pairs generally limit the photocatalytic efficiency. Doping semiconductors with heteroatoms is one of the strategies to narrow their bandgap energies and therefore extend the absorption of light to the visible region.[17, 18] However, foreign elements doped in semiconductor lattices can also cause stress to crystal lattice and act as undesirable carrier trapping sites. Vacancy engineering, i.e. self-doping of vacancy in semiconductors, have drawn increasing attention in the field of energy conversion and storage applications such as water splitting,[19-21] CO_2 reduction,[22-25] and solar cells.[26] It has been demonstrated as a powerful tool to manipulate various important properties of semiconductor materials including electrical conductivity, band structures and surface arrangement.[27, 28]

As photocatalytic reactions happen at the surface of the photocatalysts, the atomic arrangement of semiconductor surface significantly influences their surface properties, thus governing the selectivity and efficiency of semiconductor photocatalysts.[29-31] It has been demonstrated that control of the concentration and distribution of surface vacancy could effectively tune the band structure, surface properties and performances. However, limited research works are available concerning the effect of the density of vacancy and understanding the intrinsic properties resulted from varying the density of vacancy. Therefore, it is highly

desirable to design semiconductor photocatalysts with varied vacancy density and achieve in-depth understanding on how it affects the properties and the activity of the photocatalysts.

Two-dimensional semiconductor materials have shown attractive performances in photocatalysis.[32] Among the semiconductors studied, graphitic carbon nitride (g-C_3N_4), a two-dimensional conjugated polymer with weak van der Waals force between g-C_3N_4 layers, has been found as a promising visible-light-active photocatalyst for H_2 evolution and CO_2 reduction,[15, 33-35] due to its suitable band structure, low cost, good thermal and chemical stability, and facile preparation methods. Moreover, the polymeric nature allows the control over the surface chemistry via molecular-level modification and surface engineering.[36-38] For instance, simple heat treatment of g-C_3N_4 in reduced atmosphere such as H_2[39] and NH_3[40] can not only exfoliate the bulk g-C_3N_4 into nanosheets, but also lead to the release of surface atoms and consequently the simultaneous production of homogeneous vacancies on the surface of the exfoliated nanosheets. Thus, g-C_3N_4 can be chosen as an appropriate semiconductor to create surface vacancies with varied intensity toward mechanistic understanding of the effect of surface vacancies on photocatalytic activity.

In this work, to explore the fundamental mechanism of nitrogen vacancies on photocatalysis, g-C_3N_4 nanosheets with tunable nitrogen vacancies were prepared as the photocatalysts for H_2 evolution and CO_2 photoreduction. The combined experimental analyses and DFT calculations have revealed that the nitrogen vacancies in g-C_3N_4 induce the formation of midgap states under the conduction band edge and the position of midgap states becomes deeper with the increase of nitrogen vacancies. The nitrogen vacancies could cause the excitation of electrons into midgap states so as to absorb photons with longer wavelengths, trap photogenerated electrons to minimize the recombination loss of photogenerated electron-hole pairs, and transfer trapped

electrons to Pt co-catalyst. Further, the unique chemical environment on the surface caused by the nitrogen vacancies leads to the formation of highly dispersed an ultrasmall Pt nanoparticles (1-2 nm) on g-C_3N_4. As a result, the photocatalyst with the optimum density of nitrogen vacancies displays remarkably higher photocatalytic activities with 18 times and 4 times of enchantment for H_2 evolution and CO_2 reduction to CO, respectively. On the other hand, the over-introduction of nitrogen vacancies generates deeper midgap states as recombination centers resulting in the deterioration of photocatalytic activities. Our work provides new insight into the fundamental understanding of adjustable vacancy densities for photocatalyis.

2. RESULTS AND DISCUSSION

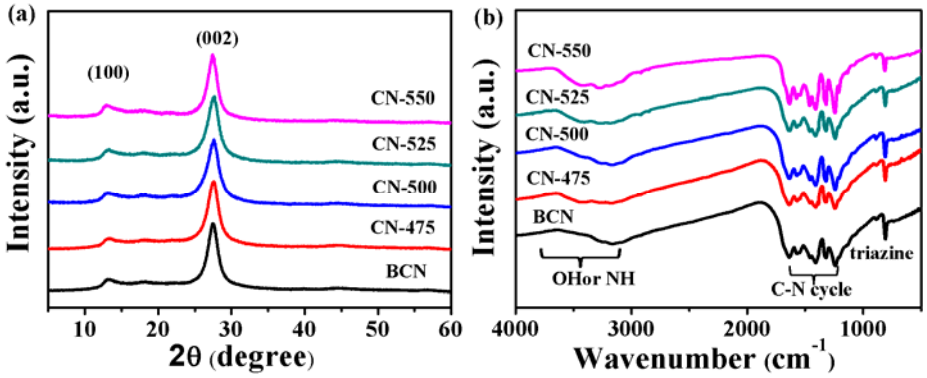

Figure 1. (a) XRD patterns and (b) FTIR spectra of bulk g-C_3N_4 (BCN) and heated treated g-C_3N_4 (CN-*x*) samples.

2.1. The characterization of g-C_3N_4 with heat treatment. The bulk g-C_3N_4 labeled as BCN was synthesized via thermal polycondensation of melamine at 550 °C for 4 h. The g-C_3N_4 nanosheets with varied density of nitrogen vacancies were prepared by heating the BCN at temperatures ranged from 475 to 550 °C under H_2 atmosphere, and the corresponding samples were labeled as CN-*x* where *x* refers to the heat treatment temperature (CN-475, CN-500, CN-

525, and CN-550). The X-ray diffraction (XRD) patterns of all samples (**Figure 1a**) clearly show the two typical diffraction peaks at 13.2 °C and 27.4 °C which are respectively associated to the in-plane structural packing motifs of tri-*s*-triazine units (**Figure S1**) and the interlayer stacking of conjugated aromatic systems.[41] As shown in the Fourier transform infrared (FTIR) spectra (**Figure 1b**), the characteristic absorption bands of all samples (3000-3500 cm^{-1} for O–H or N–H stretching, 1200-1700 cm^{-1} for stretching of CN heterocycles, 805 cm^{-1} for stretching of triazine units) indicate the formation of g-C_3N_4.[42] No obvious changes among the samples can be observed. Therefore, it is confirmed that the basic atomic structure of g-C_3N_4 still maintains after post-heating treatment.

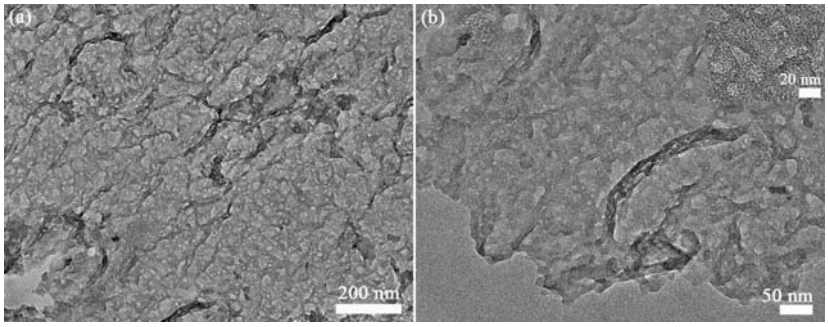

Figure 2. TEM images of CN-525. **[frame the inset picture with white lines; make the font size of labels bigger]**

The transmission electron microscopy (TEM) images of CN-525 reveal that the sample consists of thin, porous and flexible sheet-like nanostructures (**Figure 2**). As shown in the inset of Figure 2, the pores with an average diameter of about 20 nm can be observed on g-C_3N_4 nanosheets. The porosity and Brunauer-Emmett-Teller (BET) surface area were measured by nitrogen physisorption method (**Figure S2**). The nitrogen adsorption-desorption isotherms of all samples display type IV curves with a H3 hysteresis loop, indicating the presence of mesopores.[43] After post-heat treatment, the total pore volume and the BET surface area gradually

increase from 0.19 cm^3 g^{-1} and 21.45 m^2 g^{-1} of BCN to 0.78 cm^3 g^{-1} and 89.2 m^2 g^{-1} of CN-550, respectively. The enhancement of pore volume and BET surface area should be originated from the exfoliation of BCN into nanosheets with etched in-plane pores, which could offer abundant edges as active sites and channels for mass transfer during photocatalytic reactions.

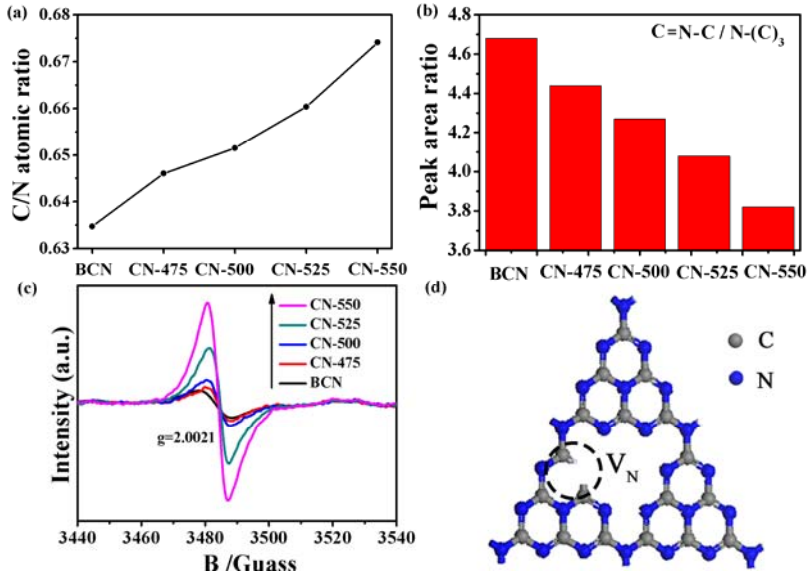

Figure 3. (a) C/N atomic ratio of BCN and CN-*x* from element analysis. (b) The peak area ratio of C=N-C groups to N-$(C)_3$ of BCN and CN-*x* from XPS analysis. (c) EPR spectra of BCN and CN-*x*. (d) The schematic of g-C_3N_4 with nitrogen vacancies. make the font size of labels bigger

2.2. Identification of tunable nitrogen vacancies confined in g-C_3N_4. In order to confirm the generation of tunable nitrogen vacancies confined in g-C_3N_4 nanosheets, three complementary analytical methods were used. Firstly, elemental analysis shows that C/N atomic ratio gradually increases from 0.635 in BCN to 0.674 in CN-550 as the heat treatment temperature was increased, implying the gradual release of nitrogen species from g-C_3N_4 and the growing number of nitrogen vacancies (**Figure 3a**). It is noted that the C/N ratio of g-C_3N_4 obtained from thermal condensation of melamine is generally lower than the stoichiometric ratio of 0.75 in ideal g-C_3N_4. This is due to the residual amino groups originated from incomplete

condensation of the precursor, which is in agreement with the FTIR results.[44] Secondly, the X-ray photoelectron spectroscopy (XPS) study also indicates the formation of nitrogen vacancies. The N 1s spectrum of BCN can be deconvoluted to four main components including sp^2-hybridized nitrogen in triazine rings (C–N=C) (398.5eV), tertiary nitrogen N–$(C)_3$ groups (400.1 eV), N–H groups (401.1 eV), and positive charge localization in heptazine rings (404.1 eV) (**Figure S3a**).[45] The ratio of the peak area of C–N=C group to N–$(C)_3$ gradually decreases from 4.68 (BCN) to 3.82 (CN-550) with the increasing temperature, suggesting that the loss of nitrogen atoms probably occurs at the two-coordinated lattice sites during the thermal reduction process（**Figure 3b**). Finally, the electron paramagnetic resonance (EPR) spectroscopy can provide fingerprint evidences for probing the surface vacancies in semiconductor photocatalysts. As shown in **Figure 3c**, all samples display a single Lorentzian line with the *g* value of 2.0021 in the magnetic field from 3440 to 3530 G, which is associated with the unpaired electrons of sp^2-carbon atoms within π-conjugated aromatic rings.[46] Be analogous to the role of oxygen vacancies on TiO_2 surface that donate excess unpaired electrons to Ti atoms and subsequently reduce Ti^{4+} to Ti^{3+} paramagnetic species,[47] the formation of two-coordinated nitrogen vacancies also could donate unpaired electrons to adjacent sp^2-carbon atoms within π-conjugated aromatic rings in g-C_3N_4. Compared to BCN with an almost negligible EPR signal, the intensity of EPR signal gradually enhances, revealing the increase of two-coordinated nitrogen vacancies generated in g-C_3N_4. Therefore, with the combined XPS, elemental analysis and EPR results, the generation of tunable nitrogen vacancies confined in g-C_3N_4 nanosheets has been confirmed (**Figure 3d**).

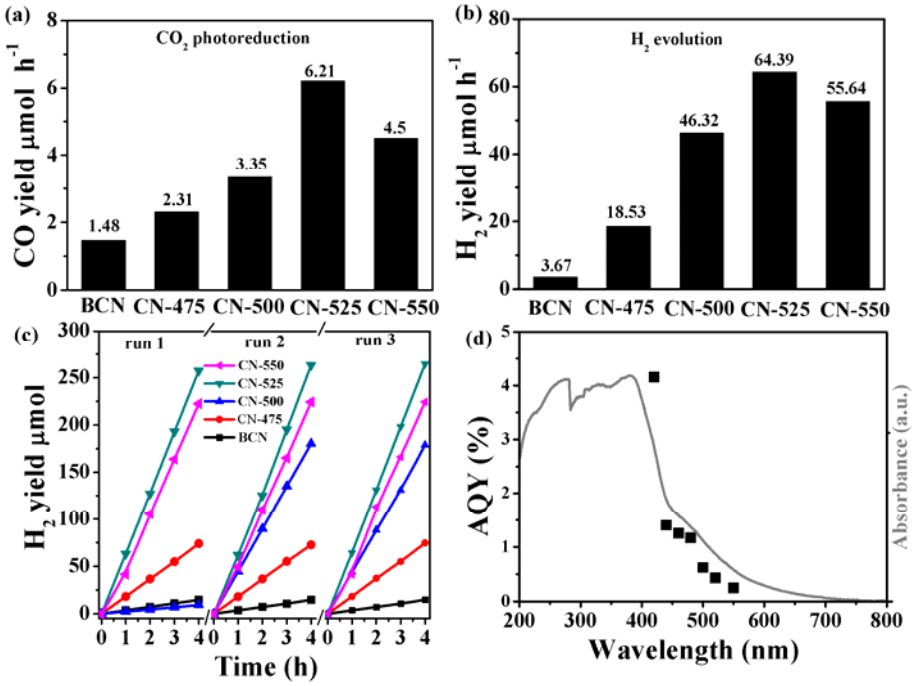

Figure 4. (a) Photocatalytic CO evolution rate over BCN and CN-*x*. (b) Photocatalytic H_2 evolution rate and (c) time course of H_2 yield over BCN and CN-*x*. (d) Wavelength dependence of H_2 evolution rate for CN-525.

2.3. Evaluation of photocatalytic performance over g-C_3N_4 with tunable nitrogen vacancies. In order to explore the relationship between the density of nitrogen vacancies in g-C_3N_4 and the photocatalytic activity, photocatalytic reduction of CO_2 and H_2 evolution reaction were conducted. As shown in **Figure 4a**, CO_2 can be reduced to CO by water vapor over both BCN and CN-*x* photocatalysts, because the CB edge of BCN and CN-*x* is at around −1.1 eV (vs normal hydrogen electrode, NHE), which is more negative than E^o (CO/CO_2) ($CO_2 + 2e^- + 2H^+ \rightarrow CO + H_2O$, E^o_{redox} = −0.53 V vs NHE). It is obvious that the CO evolution rate gradually increases with the increase of nitrogen vacancies from BCN to CN-525. The highest CO evolution rate of 6.21 μmol h^{-1} was obtained over CN-525 which is almost 4.2 times of that over BCN (1.48 μmol h^{-1}). Abundant lone pair electrons trapped in nitrogen vacancies as indicated in EPR spectra may benefit the CO_2 activation to generate CO_2^- intermediate and promote the

photoreduction of CO_2 to CO. However, an over-increase of nitrogen vacancies leads to a slight deterioration of CO evolution rate (4.5 μmol h^{-1}). It can be concluded that the nitrogen vacancies in optimum range of concentration have a positive correlation with the photocatalytic activity. The CO_2 reduction experiment performed in the dark or in the absence of the photocatalyst did not produce CO, proving that CO_2 reduction reaction is driven by light with the photocatalysts. Control experiments under UV-visible light irradiation were also performed over samples in Ar atmosphere. In the absence of CO_2, neither CO nor other carbon compounds were detected, indicating that there was no residual carbon or other carbon contamination in the system.

Splitting water into H_2 under visible light irradiation ($\lambda > 420$ nm) was also conducted with 3 wt% Pt as the co-catalyst in a water/triethanolamine solution to evaluate the effect of tunable nitrogen vacancies on photocatalysis (**Figure 4b**). It is obvious that the H_2 evolution rate also shows the same trend as the CO evolution rate, which confirms that the introduction of vacancies enhances the photocatalytic activity, but it should be controlled in an appropriate range. CN-525 achieves the highest H_2 evolution rate of 64.39 μmol h^{-1}, which is around 18 times of that over BCN. Consistent with the trend in CO_2 reduction, a further increase of nitrogen vacancies in CN-550 leads to lowering the H_2 evolution rate to 55.64 μmol h^{-1}. The H_2 evolution rate of all samples displays no obvious decrease after three consecutive runs (**Figure 4c**), indicating good stability and reusability of photocatalysts against photocorrosion. Wavelength-dependent H_2 evolution reveals the activity of CN-525 matches its optical absorption spectrum (**Figure 4d**), thus suggesting that the H_2 production is primarily driven by photoinduced electrons in g-C_3N_4. The calculated apparent quantum efficiency (AQE) of CN-525 is 4.2% at 420 nm.

2.4. Mechanistic insights of the influence of tunable nitrogen vacancies on photocatalysis.

The photocatalytic efficiency is usually determined by the balance of thermodynamics and

kinetics of light-harvesting processes, charge transport and separation processes, and catalytic reaction processes. Therefore, we explore the effect of tunable nitrogen vacancies on photocatalysis from these aspects.

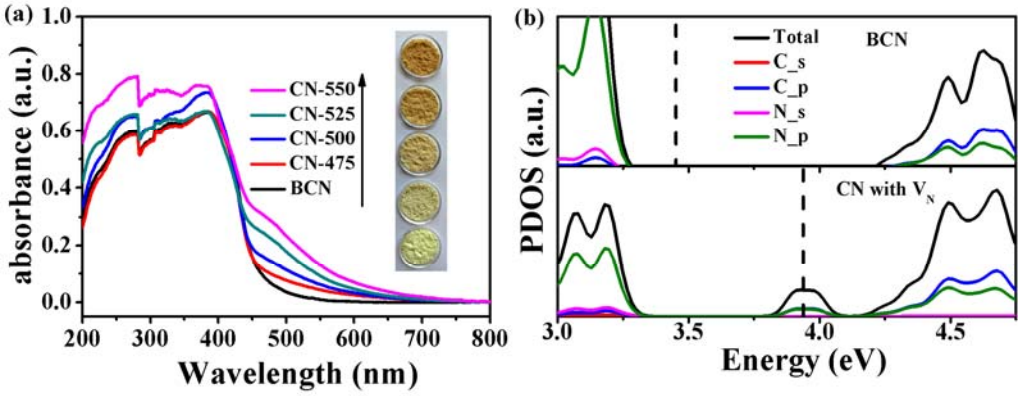

Figure 5. (a) UV-visible absorption spectra of BCN and CN-*x*, and the photographs of the samples (the inset). (b) Calculated PDOS of BCN and g-C_3N_4 (CN) with nitrogen vacancies (V_N).

2.4.1. Analysis of light-harvesting and band structure. Compared to BCN, g-C_3N_4 nanosheets with nitrogen vacancies exhibit extended visible light absorption with wide shoulder tail (Urbach tail), and the edge of the Urbach tail gradually red-shifts in the visible light range when increasing the density of nitrogen vacancies, as evidenced by the changing color of the samples from light yellow to yellow-brown (Figure 5a). Usually, the Urbach tail is attributed to the electronic states located within the band gap (known as midgap states).[48] The electronic structure of g-C_3N_4 nanosheets with nitrogen vacancies was studied using periodic density functional theory (DFT) (Figure 5b). The band gap of pristine g-C_3N_4 calculated by the generalized gradient approximation (GGA[49]) in the scheme of Perdew-Bueke-Ernzerh (PBE[50]) function is 1.03 eV, which is much smaller than the experimental value (2.7 eV), owing to the well-known limitation of DFT.[51, 52] Compared with the calculated local partial density of states (PDOS) of BCN, new midgap states appear near the bottom of conductive band (CB) in g-C_3N_4

with nitrogen vacancies. It is theoretically revealed that the loss of nitrogen atoms in π-conjugated aromatic rings of g-C_3N_4 results in the reconstruction of band structure.

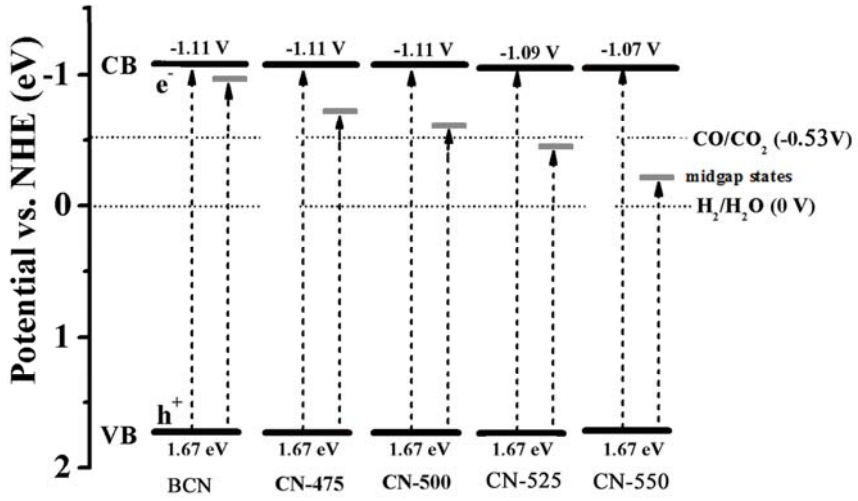

Figure 6. Schematic illustration of the electronic structure of BCN and CN-*x*. The gray dark lines refer to the band edge of midgap states, and a series of midgap states exist below the CB.

In order to acquire the position of midgap states, the band gap (E_g) energies of all the samples were transformed from the absorption spectra with the Kubelk–Munk method (**Figure S4**). There is no obvious difference in the band gap energy of all the heat-treated CN-*x* samples from that of the pristine BCN sample of around 2.7 eV. The band tails of the midgap states can be estimated to a first approximation by plotting the absorption edge data using the equation originally given by Urbach,[53] which is expressed as:

$$\alpha = \alpha_0 \exp(h\nu / Eu) \quad (1)$$

where α is absorption coefficient, α_0 is a constant, $h\nu$ is the incident photon energy, and *Eu* denotes the energy of the band tail or sometimes called the Urbach energy. The inset of **Figure S4** shows Urbach plots of all samples. The *Eu* values were calculated from the inverse of the slope of *Ln* α versus (*hv*). The *Eu* values gradually increase from 0.18 eV to 0.844 eV with more

abundant nitrogen vacancies, which is consistent with UV-visible absorption spectra. It is expected that the midgap states of BCN are originated from the defects in g-C_3N_4. Combining with the unchanged VB position from XPS valence band spectra (**Figure S3b**), the band edge of midgap states could be approximately determined and are shown in **Figure 6.** As the midgap states are close to the edge of CB, the electrons can be more easily excited from VB to midgap states. As shown in **Figure 4d**, CN-525 also exhibits AQE of 1.26% at 460 nm, 0.62% at 500 nm, and 0.25% at 550 nm, but BCN is inactive under irradiation of phones with wavelengths longer than 460 nm, revealing that photons with longer wavelengths could excite electrons into midgap states of CN-525 for enhanced H_2 evolution. Based on the above results, it is found that increasing nitrogen vacancies in g-C_3N_4 induces the formation of deeper midgap states to accommodate more charge carriers excited by photons of longer wavelengths.

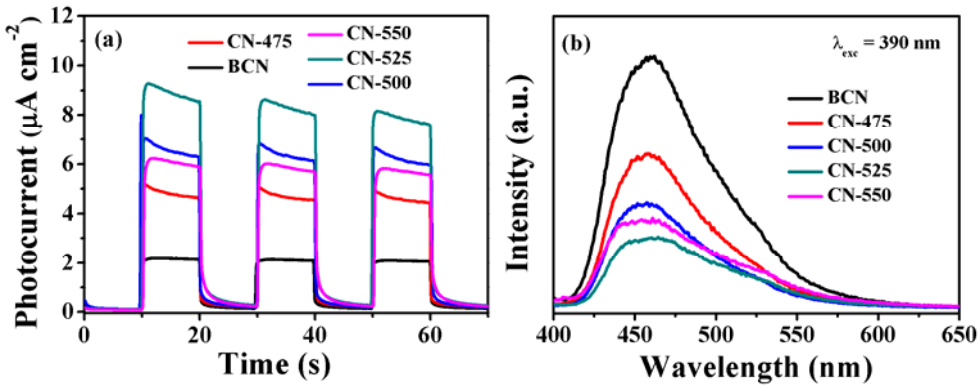

Figure 7. (a) Photocurrent responses and (b) PL emission spectra of BCN and CN-*x*.

2.4.2. Charge separation and transportation. To prove the positive impact of nitrogen vacancies on separation and transportation of photogenerated electron-hole pairs under irradiation, the periodic on/off photocurrent response was measured over the samples deposited on ITO electrode (**Figure 7a**). Photoanodes coated with CN-*x* display significant enhancement in photocurrent response compared to BCN. The photocurrents increase along with the increase of

nitrogen vacancies from CN-475 to CN-525, indicating that more photogenerated electrons in g-C_3N_4 transfer to the collecting electrode. However, further increase of nitrogen vacancies in CN-550 leads to decrease of the photocurrent, probably due to over-introduction of nitrogen vacancies acting as recombination sites. The charge separation efficiency was also investigated by photoluminescence spectra (PL) at an excitation wavelength of 390 nm (**Figure 7b**). The PL intensity decreases with the increasing nitrogen vacancies from CN-475 to CN-525, which indicates the reduced recombination of photogenerated electron-hole pairs in comparison to BCN. Such observation implies that the midgap states caused by nitrogen vacancies might be the sites for trapping photogenerated electrons, and increasingly deeper midgap states accelerate the separation of photogenerated electron-hole pairs. However, further increase of nitrogen vacancies leads to the enhancement of PL intensity (CN-550). In this case, the deeper midgap states below CB could not only trap photogenerated electrons, but also serve as sites for trapping photogenerated holes, and then become recombination sites of photogenerated electron-hole pairs. This also could explain the reason of the decreased photocurrent response of CN-550 with the enhanced light absorption. Moreover, CN-525 shows a much smaller diameter of the semicircular Nyquist curve of electrochemical impedance spectroscopy (EIS) under visible light radiation than that of BCN (**Figure 5S**), implying smaller charge transfer resistance and higher separation efficiency of photogenerated electron-hole pairs.

Therefore, the increase of nitrogen vacancies in g-C_3N_4 leads to the gradual enhancement of light-harvesting and charge transport and separation, and subsequently the increase of photocatalytic activity from CN to CN-525. However, over-introduction of nitrogen vacancies could generate the deeper midgap states that act as recombination sites which results in a deterioration of photocatalytic performance for CN-550. It is revealed that the balance of light-

harvesting and charge separation and transportation by introducing an appropriate density of nitrogen vacancies is important for optimizing the photocatalytic performance.

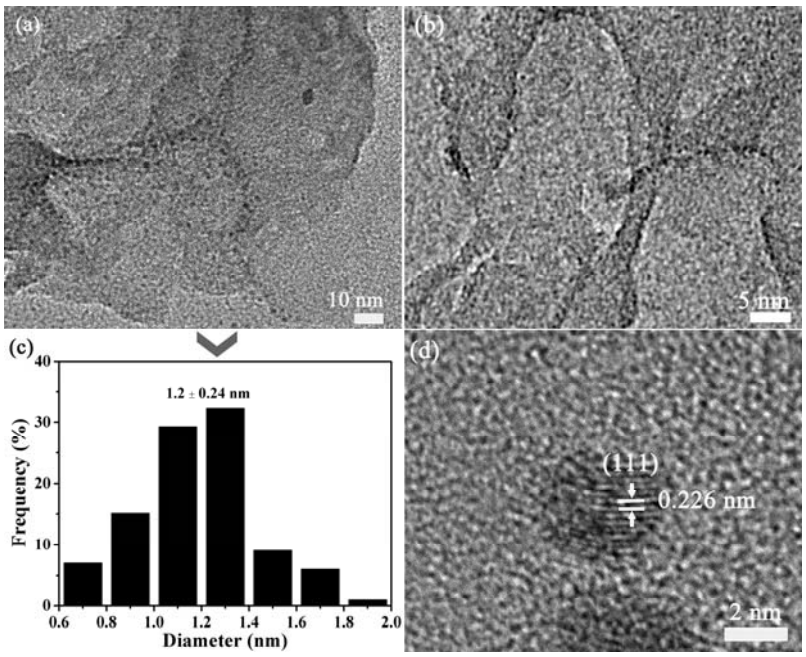

Figure 8. (a, b) TEM image, (c) Pt particle size distribution plot (number of particles: 100), and (d) high-resolution TEM images of CN-525 with 3 wt% Pt after photocatalytic reaction.

2.4.3. Catalytic reaction sites. The dispersion state of Pt co-catalyst on CN-525 was studied by TEM analysis after photocatalytic reaction. It is clearly observed that small Pt nanoparticles (appearing as dark spots) are well dispersed on g-C_3N_4 nanosheets, especially populated near the edges of the in-plane holes (**Figure 8a, b**), which reduce the opportunity for the aggregation of Pt nanoparticles. The average diameter of these nanoparticles was estimated to be 1.2 nm based on the counting of around ?? particles (**Figure 8c**). It is speculated that the unpaired electrons within π-conjugated aromatic rings on g-C_3N_4 nanosheets resulted from nitrogen vacancies can effectively reduce the adsorbed $PtCl_6^{2-}$ ions from the aqueous solution to form small Pt nanoparticles. Furthermore, nitrogen vacancies may stabilize these small particles on g-C_3N_4 nanosheets in a highly dispersed manner.[54] As single-atom heterogeneous catalysts have received

considerable attention recently, generating vacancies on nanomaterials could be one of effective methods to be explored for synthesizing single-atom heterogeneous catalysts.[55] The high-resolution TEM image (**Figure 8d**) reveals well-defined lattice fringes with an interplanar spacing of 0.226 nm, corresponding to the (111) plane of metallic Pt. Such observations show that nitrogen vacancies benefit the binding and dispersion of co-catalyst (Pt) on g-C_3N_4 and facilitate electron transfer to Pt. Therefore, nitrogen vacancies confined on g-C_3N_4 could serve as active sites to trap electrons and uniformly bind Pt nanoparticles on g-C_3N_4, thus improving the photocatalytic activities for H_2 evolution and CO_2 reduction.

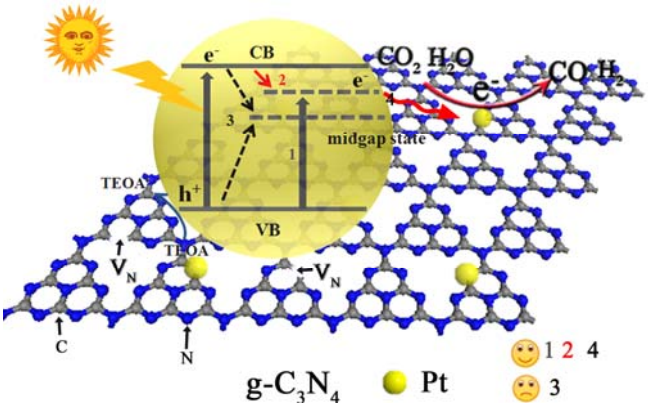

Figure 9. Schematic illustration of g-C_3N_4 with nitrogen vacancies (V_N) for photoreduction of CO_2 to CO and H_2 evolution. Paths 1, 2, 4 refer to the electron excitation from VB to midgap states, the electron trapping from conduction band to midgap states, and the electron transfer to reaction sites, respectively. Path 3 refers to deeper midgap states that act as recombination sites for trapping photogenerated electrons and holes.

Based on the above results, the mechanism of nitrogen vacancies on promoting the photocatalytic performance is proposed. As shown in **Figure 9**, the nitrogen vacancies confined in g-C_3N_4 nanosheets generate midgap states below the conduction band edge, and the position of midgap state becomes deeper with the increase of vacancy density. Under light irradiation, electrons in g-C_3N_4 can not only be excited into conduction band, but also to the midgap states by absorbing visible light with longer wavelengths (Path 1). The wavelengths of absorbed light

gradually become longer with the formation of deeper midgap states, which can excite more electron-hole pairs. Subsequently, the midgap states can also temporarily trap the excited electrons in CB to accelerate the separation of photogenerated electron-hole pairs (Path 2). However, the deeper midgap states induced by over-introduction of nitrogen vacancies could become recombination sites of photogenerated electron-hole pairs (Path 3). Finally, the excited electrons are transferred to Pt nanoparticles uniformly dispersed on g-C_3N_4 to take part in the chemical reactions (Path 4). At the optimized nitrogen vacancy density, Paths 1, 2 and 4 favorably lead to the remarkably enhanced photocatalytic activity.

3. CONCLUSION

In summary, we have explored the impact of tunable nitrogen vacancies on photocatalytic activities of g-C_3N_4 for H_2 evolution and CO_2 reduction to CO. The density of nitrogen vacancies in optimum range has a positive correlation with the photocatalytic activities, due to the gradual enhancement of light harvesting, efficient charge separation and transportation, and the uniform binding of Pt on g-C_3N_4 as active reaction sites. However, further increase of nitrogen vacancies decreases the photocatalytic activity, because the deeper midgap states induced by over-doped nitrogen vacancies could become recombination sites of photogenerated electron-hole pairs. Our work is expected to provide important new insights for fabricating nanomaterials with suitable vacancies for solar fuel generation.

4. EXPERIMENT SECTION

4.1. Sample preparation. Bulk g-C_3N_4 was prepared by heating melamine (6 g) in a semi-covered crucible to 550 °C for 4 h with a heating rate of 5 °C min^{-1} in a muffle furnace. After being cooled naturally, the yellow product was grounded in an agate mortar to obtain a powder

sample. To prepare g-C_3N_4 with different nitrogen vacancy density, the bulk g-C_3N_4 was heated to an appropriate temperature (ranging from 475 o 550 °C) for 1 h with a heating rate of 2 °C min^{-1} in hydrogen atmosphere.

4.2. Characterization. The crystal phase of the as-prepared samples was characterized by powder X-ray diffraction (XRD, Bruker D2 Phaser) equipped with a Cu-Kα radiation. The morphology of the samples was observed by field emission scanning electron microscopy (FE-SEM, JEOL JSM 6701F) and transmission electron microscopy (TEM, JEOL 3010). X-ray photoelectron spectroscopy (XPS) analysis was conducted on an AXIS-HSi spectroscope (Kratos Analytical) using a monochromated Al Kα X-ray source (1486.7 eV) and the binding energy was calibrated using the C 1s peak at 284.6 eV. The UV-visible absorption spectra were obtained on a UV-2450 spectrophotometer (Shimadazu) at room temperature. Photoluminescence (PL) spectra were collected on a Fluoromax-3 spectrometer (Horiba Scientific) at room temperature with the sample tube immersed in a quartz liquid nitrogen dewar. The specific surface area of the samples was measured by nitrogen sorption at 77K on surface area and porosity analyzer (Quantachrome Autosorb-6B, USA), and samples were degassed offline at 120 °C for 16 h under vacuum before analysis. FTIR spectra were obtained with a PerkinElmer FTIR Spectrum GX using KBr technique in the range of 4000–400 cm^{-1}. Elemental analyses for carbon and nitrogen were performed on a Vario EL III Element analyzer. Electron paramagnetic resonance (EPR) was carried out with f = 9.7688 GHz on a Bruker EMX-10/12 EPR spectrometer.

4.3. Photoelectrochemical measurement. 5 mg of photocatalysts and 10 μL of Nafion solution (5 wt%) were dispersed in 1mL of ethanol and then ultrasonically dispersed to prepare a homogeneous catalyst ink. Then, 40 μL of the catalyst ink was deposited onto an area of 0.196 cm^2 on ITO conductive glass and then was dried in air and further heated at 300 °C for 1h in

argon atmosphere to form the working electrode. Photoelectrochemical measurements were carried out in a three-electrode configuration system: a FTO working electrode, Ag/AgCl as the reference electrode, and a Pt foil as the counter electrode. Na_2SO_4 (0.5 M) aqueous solution was used as the electrolyte. The photocurrent was observed for each switch-on/off event by using a 300 W xenon lamp. An applied potential of working electrode against the counter electrode was set to 0.6 V. EIS were recorded at an applied potential of 0 V versus Ag/AgCl over the frequency range of 1 MHz to 0.1 Hz.

4.4. Photocatalytic measurement. The photocatalytic H_2 evolution reaction was conducted in a top window Pyrex cell (total volume about 300 mL with a top irradiation area of around 28 cm^2) connected to a closed gas circulation and evacuation system. In a typical run, 50 mg of the photocatalyst was dispersed in aqueous solution of TEOA (15 vol%, pH =11.0, 100 mL). Then, 3 wt% Pt as the co-catalyst was in situ photodeposited on the surface of photocatalysts. A 300 W xenon lamp equipped with a 420 nm cut-off filter (Newport) was used as the visible light source. Before light irradiation, the reaction system was evacuated and refilled with argon gas for several times to remove air and finally filled with argon gas to reach about 30 torr. The reaction cell was kept at about 20 ºC by a cooling water jacket. The produced H_2 gas was analyzed with an online gas chromatograph (Agilent 6890N, TCD detector, argon as carrier gas, 5 Å molecular sieve column). The apparent quantum efficiency (AQE) was measured under the same conditions except by replacing the 420 nm cutoff filter with a band pass interference filter (Newport) centered at 420, 440, 460,480, 500, 520, and 550 nm, respectively during the 2nd hour of the reaction. The AQE was calculated according to the following equation:

$$\mathrm{AQE} = \frac{2 \times \text{the number of evolved } H_2 \text{ molecules}}{\text{the number of incident photons}} \times 100\%$$

The photocatalytic CO_2 reduction experiments were performed in a closed circulation system by using a Pyrex cell reactor. About 50 mg of the photocatalyst was uniformly dispersed on the glass reactor with an area of 4.2 cm^2. A 300W xenon arc lamp equipped with a 420 nm cut-off filter (Newport) was used as the light source. The reaction setup was vacuum-treated several times, and then high purity of CO_2 gas (99.999%) was flowed into the reaction setup for reaching the ambient pressure. Subsequently, 0.4 mL of deionized water was injected into the reaction system as the electron donor. The as-prepared photocatalysts were allowed to equilibrate in the CO_2/H_2O atmosphere for several hours to ensure that the adsorption of gas molecules was completed. The gas products were analyzed with an online gas chromatograph (Agilent 7890a, FID detector, argon as carrier gas).

4.5. Band Structure Calculations. The DFT calculations were performed by the VASP[56, 57] code with the projected-augmented-wave (PAW[58]) method. For the exchange-correlation functional, the generalized gradient approximation (GGA[49]) in the scheme of Perdew-Bueke-Ernzerh (PBE[50]) was used. Due to the layered structure of g-C_3N_4, the van der Waals(vdW) correction proposed by Grimme[59] was chosen because of its good description of long-range vdW interactions.[60] For C and N, the $2s^2 2p^4$ and $2s^2 2p^5$ orbitals, respectively, were treated as the conduction and valence states. The cutoff energy for basis functional is 500 eV.

The atomic structure of g-C_3N_4 is shown in Fig. S1. We firstly optimized the atomic structure of g-C_3N_4 based on the above computational parameters. Then, to simulate the nitrogen vacancy in g-C_3N_4, we further used the optimized g-C_3N_4 cell to build a 2×2×2 supercell of g-C_3N_4, which includes 96C and 128N atoms. The Gamma centered 2×2×2 meshes of k-points was adopted for the Brillouin zone integration. Due to the large size of this supercell, DFT calculations using a relative accurate computational scheme, for example the hybrid functional,

may cost a huge computational resource. We then only used the GGA-PBE method to perform all the DFT calculations. The band gap of g-C_3N_4 calculated by GGA-PBE functional is 1.03 eV, which is much smaller than the experimental value (2.7 eV), owing to the well-known limitation of DFT.[52, 61] However, we merely aim at a qualitatively comparison between the pure and nitrogen vacancy contained g-C_3N_4. The GGA-PBE scheme is expected to be accurate enough to achieve this goal.

ASSOCIATED CONTENT

Supporting Information. This material is available free of charge via the Internet at http://pubs.acs.org." Additional experimental data including the atomic structure of g-C_3N_4, nitrogen adsorption-desorption isotherms, N1s XPS spectra and XPS valence band spectra, bandgap energy analysis, and EIS spectra.

AUTHOR INFORMATION

Corresponding Author

* E-mail: rxu@ntu.edu.sg

Notes

The authors declare no competing financial interests.

ACKNOWLEDGMENT

The authors acknowledge the financial support from Nanyang Technological University Cambridge Centre for Carbon Reduction in Chemical Technology (C4T) CREATE Programmes.

REFERENCES

(1) Fujishima, A.; Honda, K., Electrochemical Photolysis of Water at a Semiconductor Electrode. *Nature* **1972,** *238*, 37-38.

(2) Inoue, T.; Fujishima, A.; Konishi, S.; Honda, K., Photoelectrocatalytic Reduction of Carbon-Dioxide in Aqueous Suspensions of Semiconductor Powders. *Nature* **1979,** *277*, 637-638.

(3) Tong, H.; Ouyang, S. X.; Bi, Y. P.; Umezawa, N.; Oshikiri, M.; Ye, J. H., Nano-photocatalytic Materials: Possibilities and Challenges. *Adv. Mater.* **2012,** *24*, 229-251.

(4) Tu, W. G.; Zhou, Y.; Zou, Z. G., Photocatalytic Conversion of CO_2 into Renewable Hydrocarbon Fuels: State-of-the-Art Accomplishment, Challenges, and Prospects. *Adv. Mater.* **2014,** *26*, 4607-4626.

(5) Xu, Y.; Kraft, M.; Xu, R., Metal-free carbonaceous electrocatalysts and photocatalysts for water splitting. *Chem. Soc. Rev.* **2016,** *45*, 3039-3052.

(6) Yuan, Y.-J.; Yu, Z.-T.; Chen, D.-Q.; Zou, Z.-G., Metal-complex chromophores for solar hydrogen generation. *Chem. Soc. Rev.* **2017,** *46*, 603-631.

(7) Xiang, Q. J.; Yu, J. G.; Jaroniec, M., Synergetic Effect of MoS_2 and Graphene as Cocatalysts for Enhanced Photocatalytic H_2 Production Activity of TiO_2 Nanoparticles. *J. Am. Chem. Soc.* **2012,** *134*, 6575-6578.

(8) Zuo, F.; Bozhilov, K.; Dillon, R. J.; Wang, L.; Smith, P.; Zhao, X.; Bardeen, C.; Feng, P. Y., Active Facets on Titanium(III)-Doped TiO_2: An Effective Strategy to Improve the Visible-Light Photocatalytic Activity. *Angew. Chem. Int. Edit.* **2012,** *51*, 6223-6226.

(9) Xu, H.; Reunchan, P.; Ouyang, S. X.; Tong, H.; Umezawa, N.; Kako, T.; Ye, J. H., Anatase TiO_2 Single Crystals Exposed with High-Reactive {111} Facets Toward Efficient H_2 Evolution. *Chem. Mater.* **2013,** *25*, 405-411.

(10) Yin, P. F.; Ling, T.; Lu, Y. R.; Xu, Z. W.; Qiao, S. Z.; Du, X. W., CdS Nanoflake Arrays for Highly Efficient Light Trapping. *Adv. Mater.* **2015,** *27*, 740-745.

(11) Ran, J.; Gao, G.; Li, F.-T.; Ma, T.-Y.; Du, A.; Qiao, S.-Z., Ti_3C_2 MXene co-catalyst on metal sulfide photo-absorbers for enhanced visible-light photocatalytic hydrogen production. *Nat. Commun.* **2017,** *8*, 13907-13916.

(12) Yin, S.; Han, J.; Zou, Y.; Zhou, T.; Xu, R., A highly efficient noble metal free photocatalytic hydrogen evolution system containing MoP and CdS quantum dots. *Nanoscale* **2016,** *8*, 14438-14447.

(13) Liu, Q.; Zhou, Y.; Kou, J.; Chen, X.; Tian, Z.; Gao, J.; Yan, S.; Zou, Z., High-Yield Synthesis of Ultralong and Ultrathin Zn_2GeO_4 Nanoribbons toward Improved Photocatalytic Reduction of CO_2 into Renewable Hydrocarbon Fuel. *J. Am. Chem. Soc.* **2010,** *132*, 14385-14387.

(14) Zhang, N.; Ouyang, S.; Li, P.; Zhang, Y.; Xi, G.; Kako, T.; Ye, J., Ion-exchange synthesis of a micro/mesoporous Zn_2GeO_4 photocatalyst at room temperature for photoreduction of CO_2. *Chem. Comm.* **2011,** *47*, 2041-2043.

(15) Wang, X. C.; Maeda, K.; Thomas, A.; Takanabe, K.; Xin, G.; Carlsson, J. M.; Domen, K.; Antonietti, M., A metal-free polymeric photocatalyst for hydrogen production from water under visible light. *Nat. Mater.* **2009,** *8*, 76-80.

(16) Zheng, D.; Cao, X.-N.; Wang, X., Precise Formation of a Hollow Carbon Nitride Structure with a Janus Surface To Promote Water Splitting by Photoredox Catalysis. *Angew. Chem. Int. Edit.* **2016,** *55*, 11512-11516.

(17) Liu, G.; Wang, L.; Yang, H. G.; Cheng, H.-M.; Lu, G. Q., Titania-based photocatalysts-crystal growth, doping and heterostructuring. *J. Mater. Chem.* **2010,** *20*, 831-843.

(18) Asahi, R.; Morikawa, T.; Irie, H.; Ohwaki, T., Nitrogen-Doped Titanium Dioxide as Visible-Light-Sensitive Photocatalyst: Designs, Developments, and Prospects. *Chem. Rev.* **2014,** *114*, 9824-9852.

(19) Gordon, T. R.; Cargnello, M.; Paik, T.; Mangolini, F.; Weber, R. T.; Fornasiero, P.; Murray, C. B., Nonaqueous Synthesis of TiO_2 Nanocrystals Using TiF_4 to Engineer Morphology, Oxygen Vacancy Concentration, and Photocatalytic Activity. *J. Am. Chem. Soc.* **2012,** *134*, 6751-6761.

(20) Bi, W. T.; Ye, C. M.; Xiao, C.; Tong, W.; Zhang, X. D.; Shao, W.; Xie, Y., Spatial Location Engineering of Oxygen Vacancies for Optimized Photocatalytic H_2 Evolution Activity. *Small* **2014,** *10*, 2820-2825.

(21) Lei, F. C.; Sun, Y. F.; Liu, K. T.; Gao, S.; Liang, L.; Pan, B. C.; Xie, Y., Oxygen Vacancies Confined in Ultrathin Indium Oxide Porous Sheets for Promoted Visible-Light Water Splitting. *J. Am. Chem. Soc.* **2014,** *136*, 6826-6829.

(22) Xie, K.; Umezawa, N.; Zhang, N.; Reunchan, P.; Zhang, Y. J.; Ye, J. H., Self-doped $SrTiO_{3-\delta}$ photocatalyst with enhanced activity for artificial photosynthesis under visible light. *Energ. Environ. Sci.* **2011,** *4*, 4211-4219.

(23) Xi, G. C.; Ouyang, S. X.; Li, P.; Ye, J. H.; Ma, Q.; Su, N.; Bai, H.; Wang, C., Ultrathin $W_{18}O_{49}$ Nanowires with Diameters below 1 nm: Synthesis, Near-Infrared Absorption, Photoluminescence, and Photochemical Reduction of Carbon Dioxide. *Angew. Chem. Int. Edit.* **2012,** *51*, 2395-2399.

(24) Li, P.; Zhou, Y.; Tu, W. G.; Wang, R.; Zhang, C. F.; Liu, Q.; Li, H. J.; Li, Z. D.; Dai, H.; Wang, J. J.; Yan, S. C.; Zou, Z. G., Synthesis of $Bi_6Mo_2O_{15}$ sub-microwires via a molten salt method and enhancing the photocatalytic reduction of CO_2 into solar fuel through tuning the surface oxide vacancies by simple post-heating treatment. *CrystEngComm* **2013,** *15*, 9855-9858.

(25) Zhao, Y. F.; Chen, G. B.; Bian, T.; Zhou, C.; Waterhouse, G. I. N.; Wu, L. Z.; Tung, C. H.; Smith, L. J.; O'Hare, D.; Zhang, T. R., Defect-Rich Ultrathin ZnAl-Layered Double Hydroxide Nanosheets for Efficient Photoreduction of CO_2 to CO with Water. *Adv. Mater.* **2015,** *27*, 7824-7831.

(26) Battaglia, C.; Yin, X.; Zheng, M.; Sharp, I. D.; Chen, T.; McDonnell, S.; Azcatl, A.; Carraro, C.; Ma, B.; Maboudian, R.; Wallace, R. M.; Javey, A., Hole Selective MoO_x Contact for Silicon Solar Cells. *Nano Letters* **2014,** *14*, 967-971.

(27) Liu, Y.; Xiao, C.; Li, Z.; Xie, Y., Vacancy Engineering for Tuning Electron and Phonon Structures of Two-Dimensional Materials. *Adv. Energy Mater.* **2016**, *6*, 1600436-1600450.

(28) Li, G.; Blake, G. R.; Palstra, T. T. M., Vacancies in functional materials for clean energy storage and harvesting: the perfect imperfection. *Chem. Soc. Rev.* **2017**, *46*, 1693-1706 .

(29) Chen, X. B.; Li, C.; Gratzel, M.; Kostecki, R.; Mao, S. S., Nanomaterials for renewable energy production and storage. *Chem. Soc. Rev.* **2012,** *41*, 7909-7937.

(30) Liu, G.; Wang, L. Z.; Yang, H. G.; Cheng, H. M.; Lu, G. Q., Titania-based photocatalysts-crystal growth, doping and heterostructuring. *J. Mater. Chem.* **2010,** *20*, 831-843.

(31) Wen, F. Y.; Li, C., Hybrid Artificial Photosynthetic Systems Comprising Semiconductors as Light Harvesters and Biomimetic Complexes as Molecular Cocatalysts. *Acc. Chem. Res.* **2013,** *46*, 2355-2364.

(32) Ten Elshof, J. E.; Yuan, H. Y.; Rodriguez, P. G., Two-Dimensional Metal Oxide and Metal Hydroxide Nanosheets: Synthesis, Controlled Assembly and Applications in Energy Conversion and Storage. *Adv. Energy Mater.* **2016,** *6,* 1600355-1600388.

(33) Cao, S. W.; Low, J. X.; Yu, J. G.; Jaroniec, M., Polymeric Photocatalysts Based on Graphitic Carbon Nitride. *Adv. Mater.* **2015,** *27*, 2150-2176.

(34) Ong, W. J.; Tan, L. L.; Ng, Y. H.; Yong, S. T.; Chai, S. P., Graphitic Carbon Nitride (g-C_3N_4)-Based Photocatalysts for Artificial Photosynthesis and Environmental Remediation: Are We a Step Closer To Achieving Sustainability? *Chem. Rev.* **2016,** *116*, 7159-7329.

(35) Sun, J. H.; Zhang, J. S.; Zhang, M. W.; Antonietti, M.; Fu, X. Z.; Wang, X. C., Bioinspired hollow semiconductor nanospheres as photosynthetic nanoparticles. *Nat. Commun.* **2012,** *3*, 1139-11386.

(36) Liu, G.; Zhao, G.; Zhou, W.; Liu, Y.; Pang, H.; Zhang, H.; Hao, D.; Meng, X.; Li, P.; Kako, T.; Ye, J., In Situ Bond Modulation of Graphitic Carbon Nitride to Construct p–n Homojunctions for Enhanced Photocatalytic Hydrogen Production. *Adv. Funct. Mater.* **2016,** *26*, 6822-6829.

(37) Lau, V. W. H.; Moudrakovski, I.; Botari, T.; Weinberger, S.; Mesch, M. B.; Duppel, V.; Senker, J.; Blum, V.; Lotsch, B. V., Rational design of carbon nitride photocatalysts by identification of cyanamide defects as catalytically relevant sites. *Nat. Commun.* **2016,** *7*, 12165.

(38) Hong, J. D.; Yin, S. M.; Pan, Y. X.; Han, J. Y.; Zhou, T. H.; Xu, R., Porous carbon nitride nanosheets for enhanced photocatalytic activities. *Nanoscale* **2014,** *6*, 14984-14990.

(39) Niu, P.; Yin, L. C.; Yang, Y. Q.; Liu, G.; Cheng, H. M., Increasing the Visible Light Absorption of Graphitic Carbon Nitride (Melon) Photocatalysts by Homogeneous Self-Modification with Nitrogen Vacancies. *Adv. Mater.* **2014,** *26*, 8046-8052.

(40) Liang, Q. H.; Li, Z.; Huang, Z. H.; Kang, F. Y.; Yang, Q. H., Holey Graphitic Carbon Nitride Nanosheets with Carbon Vacancies for Highly Improved Photocatalytic Hydrogen Production. *Adv. Funct. Mater.* **2015,** *25*, 6885-6892.

(41) Yan, S. C.; Li, Z. S.; Zou, Z. G., Photodegradation of Rhodamine B and Methyl Orange over Boron-Doped g-C_3N_4 under Visible Light Irradiation. *Langmuir* **2010,** *26*, 3894-3901.

(42) Xu, J.; Zhang, L. W.; Shi, R.; Zhu, Y. F., Chemical exfoliation of graphitic carbon nitride for efficient heterogeneous photocatalysis. *J. Mater. Chem. A.* **2013,** *1*, 14766-14772.

(43) Tu, W. G.; Zhou, Y.; Liu, Q.; Yan, S. C.; Bao, S. S.; Wang, X. Y.; Xiao, M.; Zou, Z. G., An In Situ Simultaneous Reduction-Hydrolysis Technique for Fabrication of TiO_2-Graphene 2D Sandwich-Like Hybrid Nanosheets: Graphene-Promoted Selectivity of Photocatalytic-Driven Hydrogenation and Coupling of CO_2 into Methane and Ethane. *Adv. Funct. Mater.* **2013,** *23*, 1743-1749.

(44) Yan, S. C.; Li, Z. S.; Zou, Z. G., Photodegradation Performance of g-C_3N_4 Fabricated by Directly Heating Melamine. *Langmuir* **2009,** *25*, 10397-10401.

(45) Zhang, J. S.; Zhang, M. W.; Yang, C.; Wang, X. C., Nanospherical Carbon Nitride Frameworks with Sharp Edges Accelerating Charge Collection and Separation at a Soft Photocatalytic Interface. *Adv. Mater.* **2014,** *26*, 4121-4126.

(46) Zhang, G. G.; Zhang, M. W.; Ye, X. X.; Qiu, X. Q.; Lin, S.; Wang, X. C., Iodine Modified Carbon Nitride Semiconductors as Visible Light Photocatalysts for Hydrogen Evolution. *Adv. Mater.* **2014,** *26*, 805-809.

(47) Liu, L. J.; Jiang, Y. Q.; Zhao, H. L.; Chen, J. T.; Cheng, J. L.; Yang, K. S.; Li, Y., Engineering Coexposed {001} and {101} Facets in Oxygen-Deficient TiO_2 Nanocrystals for Enhanced CO_2 Photoreduction under Visible Light. *ACS. Catal.* **2016,** *6*, 1097-1108.

(48) Ran, J.; Ma, T. Y.; Gao, G.; Du, X.-W.; Qiao, S. Z., Porous P-doped graphitic carbon nitride nanosheets for synergistically enhanced visible-light photocatalytic H_2 production. *Energ. Environ. Sci.* **2015,** *8*, 3708-3717.

(49) Perdew, J. P.; Chevary, J. A.; Vosko, S. H.; Jackson, K. A.; Pederson, M. R.; Singh, D. J.; Fiolhais, C., Atoms, molecules, solids, and surfaces: Applications of the generalized gradient approximation for exchange and correlation. *Phys. Rev. B* **1992,** *46*, 6671-6687.

(50) Perdew, J. P.; Burke, K.; Ernzerhof, M., Generalized Gradient Approximation Made Simple. *Phys. Rev. Lett.* **1996,** *77*, 3865-3868.

(51) Ma, X. G.; Lv, Y. H.; Xu, J.; Liu, Y. F.; Zhang, R. Q.; Zhu, Y. F., A Strategy of Enhancing the Photoactivity of g-C_3N_4 via Doping of Nonmetal Elements: A First-Principles Study. *J. Phys. Chem. C* **2012,** *116*, 23485-23493.

(52) Huang, Z. F.; Song, J. J.; Pan, L.; Wang, Z. M.; Zhang, X. Q.; Zou, J. J.; Mi, W. B.; Zhang, X. W.; Wang, L., Carbon nitride with simultaneous porous network and O-doping for efficient solar-energy-driven hydrogen evolution. *Nano Energy* **2015,** *12*, 646-656.

(53) Urbach, F., The Long-Wavelength Edge of Photographic Sensitivity and of the Electronic Absorption of Solids. *Phys. Rev.* **1953,** *92*, 1324-1324.

(54) Xi, G. C.; Ye, J. H.; Ma, Q.; Su, N.; Bai, H.; Wang, C., In Situ Growth of Metal Particles on 3D Urchin-like WO_3 Nanostructures. *J. Am. Chem. Soc.* **2012,** *134*, 6508-6511.

(55) Yang, X. F.; Wang, A. Q.; Qiao, B. T.; Li, J.; Liu, J. Y.; Zhang, T., Single-Atom Catalysts: A New Frontier in Heterogeneous Catalysis. *Accounts. Chem. Res.* **2013,** *46*, 1740-1748.

(56) Kresse, G.; Furthmuller, J., Efficiency of ab-initio total energy calculations for metals and semiconductors using a plane-wave basis set. *Comp. Mater. Sci.* **1996,** *6*, 15-50.

(57) Kresse, G.; Hafner, J., Ab initio molecular dynamics for liquid metals. *Phys. Rev. B* **1993,** *47*, 558-561.

(58) Blöchl, P. E., Projector augmented-wave method. *Phys. Rev. B* **1994,** *50*, 17953-17979.

(59) Grimme, S., Accurate description of van der Waals complexes by density functional theory including empirical corrections. *J. Comput. Chem.* **2004,** *25*, 1463-1473.

(60) Geng, W.; Zhao, X.; Liu, H.; Yao, X., Influence of Interface Structure on the Properties of ZnO/Graphene Composites: A Theoretical Study by Density Functional Theory Calculations. *J. Phys. Chem. C* **2013,** *117*, 10536-10544.

(61) Ma, X.; Lv, Y.; Xu, J.; Liu, Y.; Zhang, R.; Zhu, Y., A Strategy of Enhancing the Photoactivity of g-C_3N_4 via Doping of Nonmetal Elements: A First-Principles Study. *J. Phys. Chem. C* **2012,** *116*, 23485-23493.

Exploring the fundamental mechanism of nitrogen vacancies confined in g-C_3N_4 nanosheets on photocatalysis when manipulating the density of vacancy in semiconductors, during which suitable nitrogen vacancies can regulate the energy band gap to enhance visible light absorption, trap photogenerated electrons, and serve as active sites to uniformly bind Pt on g-C_3N_4, thus resulting in enhancement of visible-light-driven solar fuel synthesis. However, over-introduction of nitrogen vacancies generates the deeper midgap states as recombination centers resulting in deterioration of photocatalytic activities.